stress, the post-damage elastic modulus of the material decreases, mainly resulted from the brittle properties of the material.

The interfacial bond strength and particle strength of the refractory are greater than the matrix phase strength. The damage process of the refractory material at normal temperature is divided into three stages: initial damage, matrix damage and material damage. In this experiment, the refractories were compressed and loaded at room temperature, 300 °C and 600 °C respectively. The stress-strain relationship of the refractory at 300 °C and 600 °C is expressed as:

300℃:

$$\sigma=1.369\times10^{11}\varepsilon^4+1.2387\times10^{9}\varepsilon^3+3.4260\times10^{6}\varepsilon^2+8.2359\times10^{3}\varepsilon-14.63 \quad (1)$$

600℃:

$$\sigma=4.591\times10^{10}\varepsilon^4+5.618\times10^{8}\varepsilon^3+1.032\times10^{6}\varepsilon^2+5.269\times10^{3}\varepsilon-33.12 \quad (2)$$

The Young's modulus-strain relationship is calculated as:

300℃:

$$E=5.623\times10^{8}\varepsilon^3+3.5677\times10^{6}\varepsilon^2+6.5914\times10^{3}\varepsilon+9.688 \quad (3)$$

600℃:

$$E=3.6289\times10^{8}\varepsilon^3+1.7922\times10^{6}\varepsilon^2+3.568\times10^{3}\varepsilon+4.92 \quad (4)$$

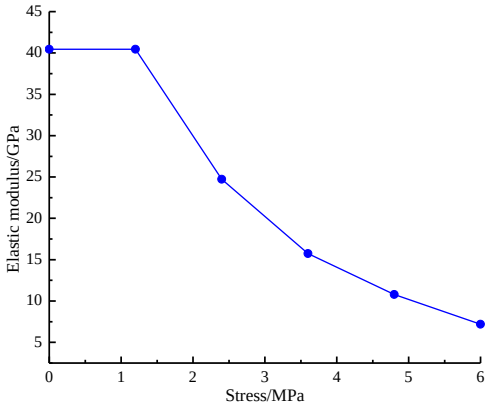

(a) Tension process

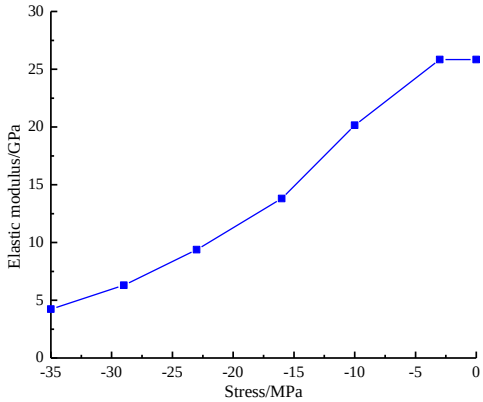

(b) Pressure process

Figure 1. Material elastic modulus with stress curve

Figure 2 shows the Young's modulus strain curve under high temperature compression. As the temperature increases, the Young's modulus of refractory decreases; the higher the temperature, the smaller the variation range of initial Young's modulus and the less reduction Young's modulus.

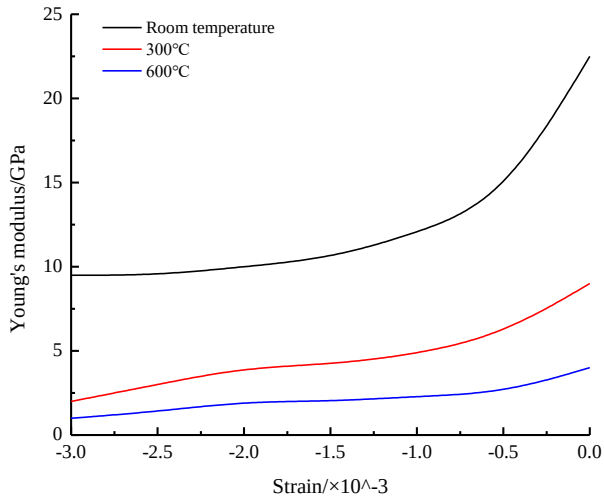

Figure 2. Young's modulus strain curve under high temperature compression

Table 1. Chemical composition and elastic modulus of two building refractories

Materials	MgO	C	Fe_2O_3	SiO_2	CaO	Al	Elastic modulus/GPa
Materials A	78.3	15.1	0.2	0.7	1.2	1.1	21.7
Materials B	90.3	6.7	0.2	0.1	2.7	—	89.1

3. CHARACTERIZATION METHOD OF MESO-DAMAGE TEST FOR TALL BUILDING REFRACTORY

3.1 Mechanical properties test

At present, the refractory for tall buildings is mainly rock wool fibre material, which is composed of rock wool fibre and mortar to isolate and protect concrete. In order to study the mechanical properties of this material, the rock wool fibre mortar was prepared by mixing 35 % rock wool fibre into the mortar. The 100mm*100mm*400mm sample was cured in the standard curing room for 28d. Three point bending mechanical test was adopted. The flexural strength and flexural modulus are expressed as:

$$F=1.5\times\frac{\Delta F\times100}{b\times h^3} \quad (5)$$

$$E=\frac{\Delta F\times L}{b\times h\times\delta} \quad (6)$$

The apparent porosity and bulk density of the RWFR were measured by a tester. They are expressed as:

$$\text{Apparent porosity: } P=\frac{m_3-m_1}{m_3-m_2}\times100\% \quad (7)$$

$$\text{Bulk density: } \rho=\frac{m_1\rho_w}{m_3-m_2} \quad (8)$$

where: m_1, m_2 and m_3 are the dry weight, the suspension weight, and the saturation weight of the samples, respectively, and ρ_w is the density of water.

Due to the incorporation of rock wool fibres, the mortar sample has a large porosity of 9.36 % and a bulk density of 2.300g/cm^3. Figure 3 shows the stress-strain curve of RWFR with the maximum stress of about 35 MPa and the maximum strain of 4.5×10^{-3}.

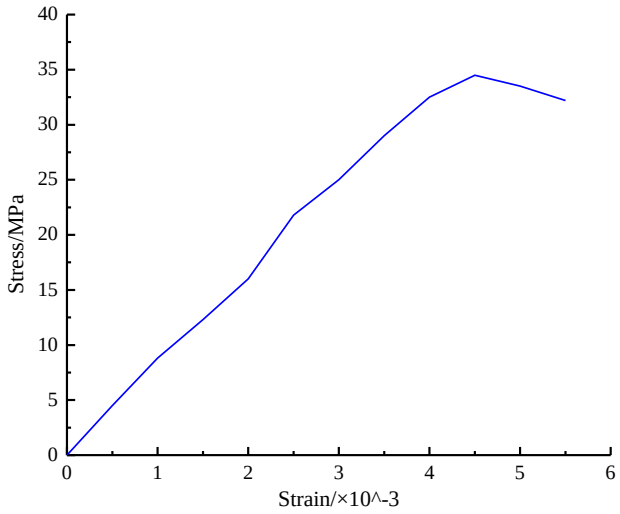

Figure 3. Stress-strain curve of rockwool mortar refractories

3.2 High temperature test

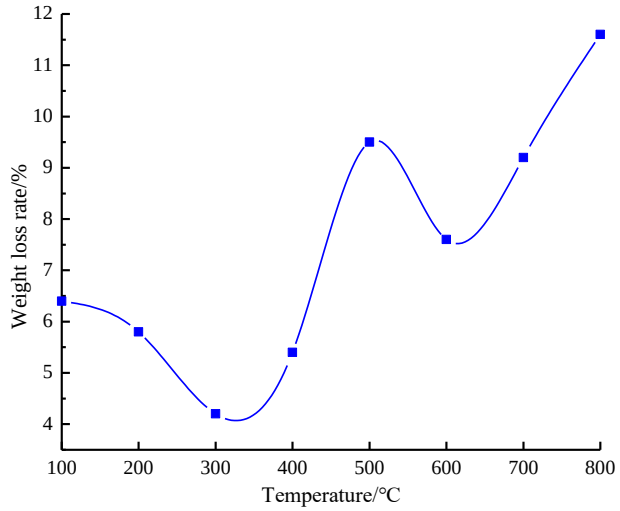

Figure 4. Test piece weight loss rate and temperature curve

For the high temperature test, the sample size was 100mm*100mm*100mm; the furnace temperature was controlled at 100 °C-800 °C, and the temperature was increased progressively by 100 °C. It was maintained in constant temperature for 60min by muffle furnace. The average number of three samples was used as the test result. Figure 4 shows the relation curve between the weight loss rate of the sample and the temperature, indicating that the weight loss of the samples at different temperatures does not increase linearly, mainly due to different sources of water loss under different temperature conditions. At the earlier stage, mainly the free water and gel water had weight loss; when the temperature rose to 400 °C, Ca $(OH)_2$ dehydration occurred; when exceeding 600 °C, the mass loss is mainly caused by the internal structure change of concrete. Figure 5 depicts the relationship between compressive strength and temperature of the samples. It can be seen that before 600 °C, the compressive strength of the RWFR decreased less; when the temperature rose to 700 °C, the strength declined to a large extent. The experiment indicates that the tested refractory material in this paper has better performance at 600 °C.

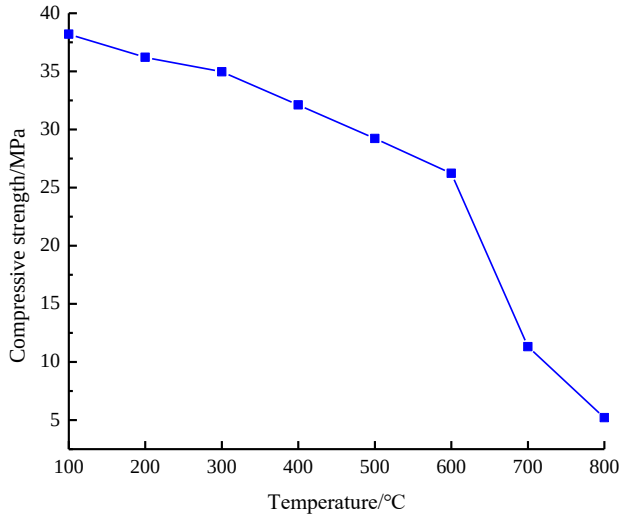

Figure 5. Test piece compressive strength and temperature curve

3.3 Analysis of meso-damage test

When the refractory material is loaded with external load, the acoustic emission can record the strain energy released during the occurrence and development of internal defects during the loading process. The damage position and development of the refractory mortar component can be clarified by means of acoustic emission technology. This test adopted a DiSP acoustic emission system with 16 acquisition channels which consists of three parts: sensor, amplifier and analysis system, to test the damage of the samples during the tri-axial loading process. In addition, the damage form of the RWFR is different, so it's necessary to characterize the compressed sample by the combination of time domain and frequency domain.

The acoustic emission signal obtained by the tri-axial loading needs to be classified using the wavelet energy spectrum coefficient. Assuming that f(t) is a wavelet transform function and ψ(t) is a wavelet base, then the wavelet transform is expressed as:

$$W_f(a,b)=\frac{1}{\sqrt{|a|}}\int_{-\infty}^{\infty} f(t)\psi\left(\frac{t-b}{a}\right)dt \quad (9)$$

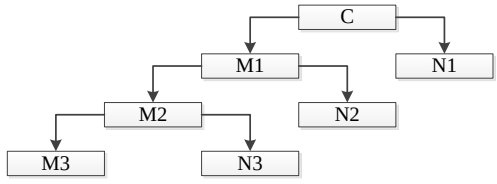

Figure 6. Wavelet transform decomposition structure diagram

In the formula above, a and b represent the discretization coefficient. After the wavelet transform, the signal is decomposed into low-frequency approximation signal and the high-frequency detail signal, and the low-frequency signal is further decomposed to obtain the tree structure, as shown in Fig. 6. Figure 7 shows an acoustic emission energy-time history of the RWFR, indicating that the damage of the samples can be roughly divided into four stages: no damage stage, slow damage development stage, damage speeding development stage and damage failure stage.

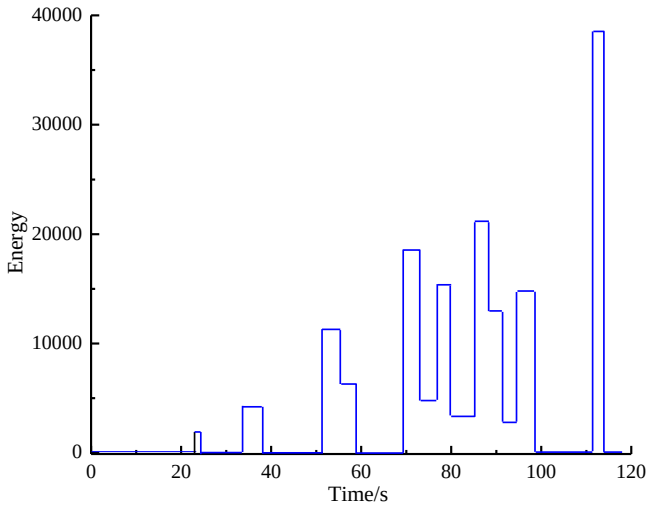

Figure 7. Acoustic emission energy-time history diagram of rock wool mortar refractory

4. DAMAGE CONSTITUTIVE MODEL OF BUILDING REFRACTORY MATERIALS

The damage of building refractory materials is manifested by the local damage of inelastic deformation. As the load increases, the inelastic deformation concentrates to the weak part of the material, while the other parts are in the elastic unloading stage. It can be seen from the damage evolution process that the damage process includes two parts: initial damage and damage evolution. At the initial damage stage, it's considered that the characteristic stress reaches the lowest strength of the internal phase in the refractory material; when entering the damage evolution stage, it's difficult to acquire the characteristic parameters of the samples, but easy for the energy parameter, which can be judged by the energy unloading relationship, as shown in Figure 8. According to this figure, the curve area represents the energy dissipation, and the value of the equivalent displacement at the end of the damage depends on the amount of energy dissipated; when the refractory is suddenly unloaded under the damaged state, the sample will recover along the OC route, but if the damage re-occurs, it will also develop along the OC route, with the damage retention function. The equivalent displacement of the initial damage is expressed as δ_{eq}^{m}; at $\delta_{eq} \geq \delta_{eq}^{0}$, the damage variable is defined as:

$$d=\frac{\delta_{eq}}{\delta_{eq}^{m}-\delta_{eq}^{0}} \quad (10)$$

The characteristics of the RWFRs studied in this paper are greatly affected by the load properties. The triaxial loading test of the samples is approximated by the calculation of compression model. Based on the Abaqus finite element software, this paper applies the damage constitutive model to the RWFR for unit compression experiment. Figure 9 shows the comparison between the experimental results and analog values. It can be found that the analog value of the constitutive model has good consistency with the test values. Because of the tension process during the actual experiment, the peak stress strain of the analog value is greater than the test values.

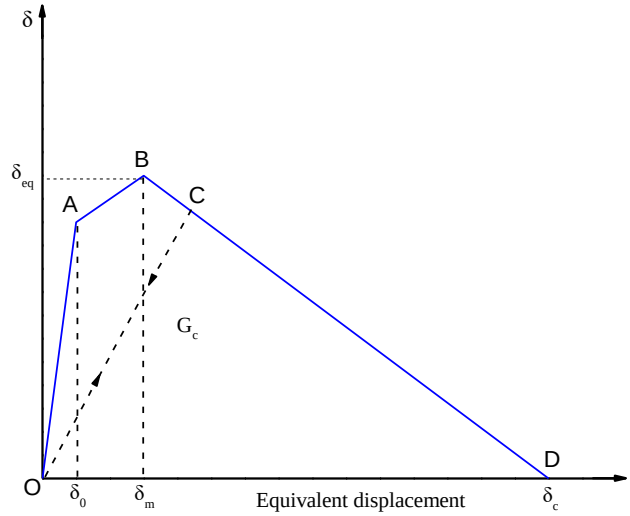

Figure 8. Energy-based unloading relationship

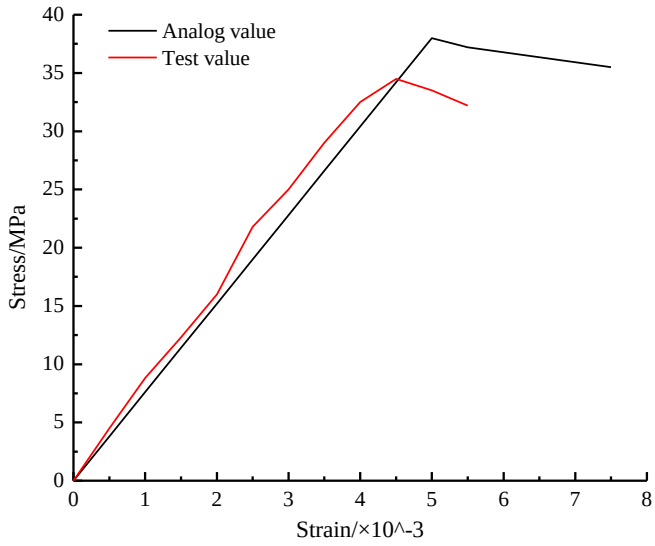

Figure 9. Comparison of experimental numerical results of refractory response

5. CONCLUSIONS

In this paper, the rock wool fibre was taken as an example of tall building refractories. On this basis, the author probed into the mechanical properties and damage evolution of the tall building refractory, and set up a meso-damage mechanics model for the material.

(1) As the temperature increases, the Young's modulus of refractory decreases; the higher the temperature, the smaller the variation range of initial Young's modulus and the less reduction Young's modulus. The maximum stress of the rock wool fibre refractory is about 35MPa, and the maximum strain is 4.5×10^{-3}.

(2) Before 600 °C, the compressive strength of the RWFR material decreases little; when the temperature rises to 700 °C, the strength decreases greatly, that is, the RWFR has a better performance at 600 °C.

(3) The damage of the RWFR can be roughly divided into four stages: no damage stage, slow damage development stage, damage speeding development stage and damage failure stage. The damage process includes two parts: initial damage and damage evolution.

(4) The damage process of building refractory includes initial damage and damage evolution. The damage is manifested by the local damage of inelastic deformation; as the load increases, the inelastic deformation concentrates to the weak part of the material, while the other parts are in the elastic unloading stage.

ACKNOWLEDGMENT

Major Projects of the Natural Fund of Hefei University in 2018 (Item number: 18ZR02ZDA).

REFERENCES

[1] Chen, X., Yang, H., Sun, K. (2016). Developing a meta-model for sensitivity analyses and prediction of building performance for passively designed high-rise residential buildings. Applied Energy, 194: 422-439. https://doi.org/10.1016/j.apenergy.2016.08.180

[2] Lu, X., Zhou, B., Zhao, B., Lu, W. (2015). Shaking table test and numerical analysis of a high-rise building with steel reinforce concrete column and reinforce concrete core tube. The Structural Design of Tall and Special Buildings, 24(18): 1019-1037. https://doi.org/10.1002/tal.1224

[3] Shim, H.B., Kim, Y., Park, H.S. (2019). Experimental tests for improving buildability of construction methods for high-strength concrete columns in high-rise buildings. The Structural Design of Tall and Special Buildings, 28(2). https://doi.org/10.1002/tal.1570

[4] Chau, C.K., Xu, J.M., Leung, T.M., Ng, W.Y. (2016). Evaluation of the impacts of end-of-life management strategies for deconstruction of a high-rise concrete framed office building. Applied Energy, 185: 1593-1603. https://doi.org/10.1016/j.apenergy.2016.01.019

[5] Pejovic, J., Jankovic, S. (2016). Seismic fragility assessment for reinforced concrete high-rise buildings in southern euro-Mediterranean zone. Bulletin of Earthquake Engineering, 14(1): 185-212. https://doi.org/10.1007/s10518-015-9812-4

[6] Zhou, X., Li, G. (2013). A macro-element based practical model for seismic analysis of steel–concrete composite high-rise buildings. Engineering Structures, 49: 91-103. https://doi.org/10.1016/j.engstruct.2012.11.002

[7] Munir, A., Warnitchai, P. (2013). Optimal reduction of inelastic seismic demands in high-rise reinforced concrete core wall buildings using energy-dissipating devices. Structural Design of Tall and Special Buildings, 22(7): 543-568. https://doi.org/10.1002/tal.704

[8] Epackachi, S., Mirghaderi, R., Esmaili, O., Behbahani A.A.T., Vahdani, S. (2012). Seismic evaluation of a 56-storey residential reinforced concrete high-rise building based on nonlinear dynamic time-history analyses. The Structural Design of Tall and Special Buildings, 21(4): 233-248. https://doi.org/10.1002/tal.586

[9] Warnitchai, P., Munir, A. (2011). Identification of reasons for high inelastic seismic demands in high rise RC core wall buildings. Procedia Engineering, 14(3): 1359-1366. https://doi.org/10.1016/j.proeng.2011.07.171

[10] Koduru, S.D., Haukaas, T. (2010). Probabilistic seismic loss assessment of a Vancouver high-rise building. Journal of Structural Engineering, 136(3): 235-245. https://doi.org/10.1061/(ASCE)ST.1943-541X.0000099

[11] Zou, D., Liu, T., Teng, J., Du, C., Li, B. (2014). Influence of creep and drying shrinkage of reinforced concrete shear walls on the axial shortening of high-rise buildings. Construction & Building Materials, 55(2): 46-56. https://doi.org/10.1016/j.conbuildmat.2014.01.034

[12] Shin, M., Kang, H.K., Lafave, J.M., Grossman, J.S. (2012). Design and behaviour of a reinforced concrete high-rise tube building with belt walls. Structural Design of Tall and Special Buildings, 21(12): 918-932. https://doi.org/10.1002/tal.661

[13] Park, H.S., Won, J.H., Chung, W.J. (2019). Wind resistance performance evaluation of cable-type curtain wall system on reinforced concrete high-rise buildings. International Journal of Concrete Structures and Materials, 12(1): 1-11. https://doi.org/10.1186/s40069-018-0320-1